OPEN ACCESS Freely available online

AFM Applied Functional Materials

ISSN 2737-5323
Volume 3, Issue 1
https://www.iikii.com.sg/journal/AFM
Applied Functional Materials

Article

Analysis of Ultra-Broadband Absorber with Multilayer Structure in Visible to Near Infrared Light

David Yang [1], Ling-Chieh Tseng [2], Wei-Zheng Li [2], and Cheng-Fu Yang [2,3,*]

[1] School of Electronic Information and Electrical Engineering, Huizhou University, Huizhou 516007, China; Davidyang@gmail.com
[2] Department of Chemical and Materials Engineering, National University of Kaohsiung, Kaohsiung 811, Taiwan; jason8802178@gmail.com (L.C. Tseng); a1095611@mail.nuk.edu.tw (W.Z. Li)
[3] Department of Aeronautical Engineering, Chaoyang University of Technology, Taichung 413, Taiwan
* Correspondence: cfyang@nuk.ecu.tw

Received: Jan 29, 2023; **Revised:** Feb 20, 2023; **Accepted:** Feb 27, 2023; **Published:** Mar 30, 2023

Abstract: We have designed an absorber with ultra-broadband absorption spanning from visible light to near-infrared light. The performance of the designed absorber was validated with numerical analysis using the COMSOL simulation software. The absorber structure consists of two layers of square cubes stacked on top of four layers of continuous flat films. Starting from the top, the structure consists of an aluminum oxide (Al_2O_3) and titanium (Ti) cube, followed by a four-layer continuous planar film consisting of poly N-isopropyl acrylamide (PNIPAAm), titanium (Ti), silicon dioxide (SiO_2), and titanium (Ti). The simulation analysis results indicated the exceptional performance of this absorber in terms of ultra-broadband. Its high absorption rate was attributed to several factors. Firstly, the top alumina layer exhibits anti-reflection properties, which minimize reflection losses. Secondly, the absorber incorporates three different resonances: local surface plasmon resonance, propagating surface plasmon resonance, and Fabry-Perot cavity resonance. These resonances coexisted within the designed absorber, and at least two of them occurred simultaneously. Thirdly, the formation of two Fabry-Perot cavities within PNIPAAm and silica dielectric layers contributed to the overall performance. The combined effects of anti-reflection, multiple resonances, and the presence of Fabry-Perot cavities enabled the absorber to achieve ultra-broadband absorption and a high absorption rate. Overall, the designed absorber demonstrated remarkable characteristics in absorbing a wide range of wavelengths, from visible light to near-infrared light, while maintaining a high absorption efficiency.

Keywords: Ultra-broadband; Absorber; COMSOL; Fabry-Perot resonator; Localized surface plasmon resonance

1. Introduction

The global energy issue has long been paramountly important worldwide with the excessive dependence on fossil fuels that pose severe threats to the environment and ecology. To mitigate these risks, the development of renewable energy sources such as solar, wind, and water has been carried out significantly. Among these alternatives, solar energy stands out due to its regenerative nature and widespread availability with extensive research and exploration. To harness solar energy more effectively, the development of efficient solar absorbers is crucial. These absorbers play a vital role in capturing and converting sunlight into usable energy. Therefore, this research was carried out to address the challenge of designing absorbers with a high absorption rate. By focusing on this objective, we optimized the utilization of solar energy to contribute to the advancement of sustainable and environmentally friendly power generation. In 2008, Landy et al. first introduced the concept of narrowband perfect absorbers, using a metal-insulator-metal (MIM) structure to achieve 100% absorption at specific frequencies [1]. This groundbreaking discovery demonstrated the effectiveness of metamaterial absorbers in efficiently capturing electromagnetic waves. Consequently, metamaterial absorbers have garnered significant attention from scholars. After extensive research and dedication of scholars, significant advancements have been made in the development of excellent absorbers. Initially limited to single-band absorption [2], researchers have successfully expanded the range to include dual-band absorption [3] and even multi-band absorption [4]. Moreover, these advancements have extended to various regions of the electromagnetic spectrum, such as ultraviolet light [5], visible light [6], near-infrared light [7], and far-infrared light [8]. As a result, perfect absorption capabilities have been achieved across a diverse range of wavelengths.

Over time, researchers have also expanded their capabilities from single-band absorption to dual-band and multi-band absorption. Moreover, they have developed absorbers successfully that have for different regions of the electromagnetic spectrum,

including ultraviolet, visible, near-infrared, and far-infrared wavelengths. Additionally, various techniques were developed to expand the bandwidth and enhance the absorption efficiency of metamaterial absorbers. These techniques leveraged localized surface plasmon resonance, Fabry-Perot resonance, and propagating surface plasmon resonance [9–11]. As a result, numerous studies have combined these different approaches to develop multilayer absorbers and investigated ultra-broadband characteristics within various wavelength ranges. This continuous research and innovation have paved the way for the development of highly efficient absorbers with wide-ranging applications.

COMSOL finite element analysis software is a powerful tool for modeling and simulating multiphysics phenomena. It allows users to define material parameters, set up complex geometries, and describe the physical fields associated with specific phenomena. By converting the engineering problem's differential equation into an integral equation and employing geometric division and variable approximation, the software transforms it into a system of simultaneous algebraic equations. These equations are then implemented in a program and solved computationally to determine the unknown variables. Over the years, numerous researchers have explored the development of absorbers with various structures and the use of stacked film layers. These endeavors aimed to achieve high absorption rates and ultra-broadband effects. By utilizing the capabilities of COMSOL, researchers could design absorbers that efficiently capture and attenuate a wide range of electromagnetic or acoustic waves across different frequencies. The software allows for accurate simulation and analysis, enabling the optimization of absorber designs to achieve desired performance characteristics.

In this study, we optimized and simulated an absorber with ultra-broadband capabilities using COMSOL finite element analysis. The absorber was designed to have a four-layer continuous planar film with an additional two layers of square cubes stacked on the top. The top layer, made of aluminum oxide square cubes, served a dual purpose as an anti-reflection and anti-corrosion layer, effectively protecting the underlying titanium square layer from oxidation. We further investigated the simultaneous excitation of local surface plasmon resonance, propagating surface plasmon resonance, and Fabry-Perot cavity resonance in the absorber to achieve high absorption across a wide spectrum of wavelengths. Additionally, two Fabry-Perot resonant cavities were created within poly N-isopropyl acrylamide (PNIPAAm) and silicon dioxide dielectric layers. Simulation results demonstrated that the innovative structure of the designed absorber exhibited a remarkable absorption rate of 90% and an average absorption rate of 96.3% over an extensive wavelength range spanning from 600 to 3650 nm. With its exceptional absorption efficiency and ultra-broadband characteristics, the designed absorber holds significant potential for diverse applications in electromagnetic stealth, solar power generation, and thermoelectric devices.

2. Experimental Parameters and Methods

Fig. 1(a) illustrates the three-dimensional structure of the absorber we have designed, comprising numerous square cubes positioned on the *x*-*y* plane. Fig. 1(b) presents a cross-sectional view of the absorber and provides information about its composition and thickness. From the top, the absorber consisted of several layers. First, there was a square cube composed of an anti-reflection layer made of aluminum oxide (Al_2O_3) and an absorbing layer made of titanium (Ti). Subsequently, the layers included a dielectric layer of PNIPAAm, an additional absorbing layer of Ti, a dielectric layer of silicon dioxide (SiO_2), and finally a substrate layer of Ti.

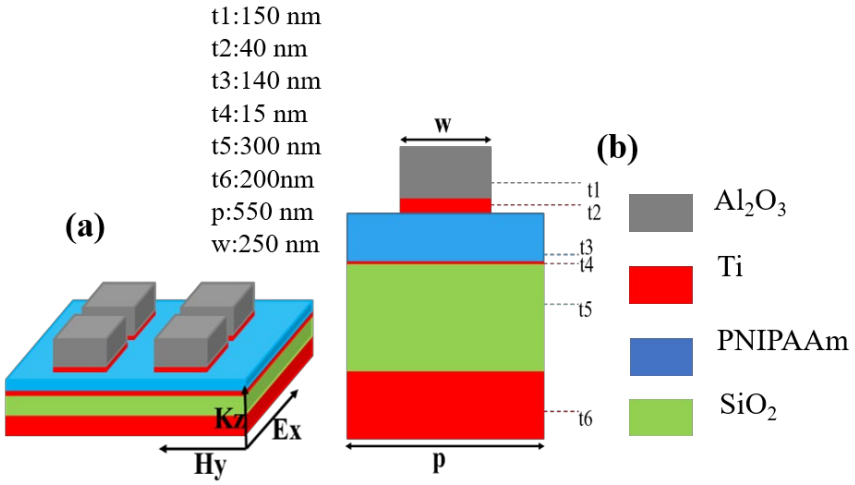

Fig. 1. (**a**) Three-dimensional structure diagram of the absorber; (**b**) Sectional view of the absorber and the thickness and material represented by each layer.

The respective thicknesses of these layers were as follows: t1 (Al_2O_3) = 150 nm, t2 (Ti) = 40 nm, t3 (PNIPAAm) = 140 nm, t4 (Ti) = 15 nm, t5 (SiO_2) = 300 nm, t6 (Ti) = 200 nm. The period of the structure, denoted as p, measures 550 nm, and the width of the uppermost square cube, referred to as w, was 250 nm. We implemented periodic boundary conditions in the *x* and *y* directions. The incident light was directed perpendicular to the absorber, following the negative *z* direction. For simulation, the polarization direction of the incident light was aligned with the *x*-axis. These parameters were chosen due to the presence of a significantly thick Ti layer at the bottom, which prevented any light transmission. As a result, the overall transmittance of the structure was zero. Therefore, when calculating the absorption rate, it was represented as A = 1 − R, where A denotes the absorption rate.

3. Results

To demonstrate that a square cube with a length (w) of 250 nm was an optimal choice for the structure, we simulated and analyzed various side lengths ranging from 200 to 260 nm with 10 nm intervals. Fig. 2 illustrates the results of the simulation, revealing absorption peaks at 490, 610, 820, 1170, and 2280 nm in the absorption spectrum. By examining these findings, we determined that for cube lengths of 220, 230, 240, 250, and 260 nm, the corresponding wavelength ranges with absorption rates above 90% were 600 to 3450 nm, 600 to 3500 nm, 600 to 3570 nm, 600 to 3650 nm, and 600 to 3700 nm. These results indicated that as the cube's side length increased from 220 to 260 nm, the wavelengths within the low band where the absorption rate exceeded 90%, remained relatively consistent. Conversely, the wavelengths within the high band where the absorption rate surpassed 90%, shifted from 3450 to 3700 nm. This behavior enabled the superior performance of the designed ultra-broadband absorber, which exhibited a high absorption rate across a wide range of wavelengths.

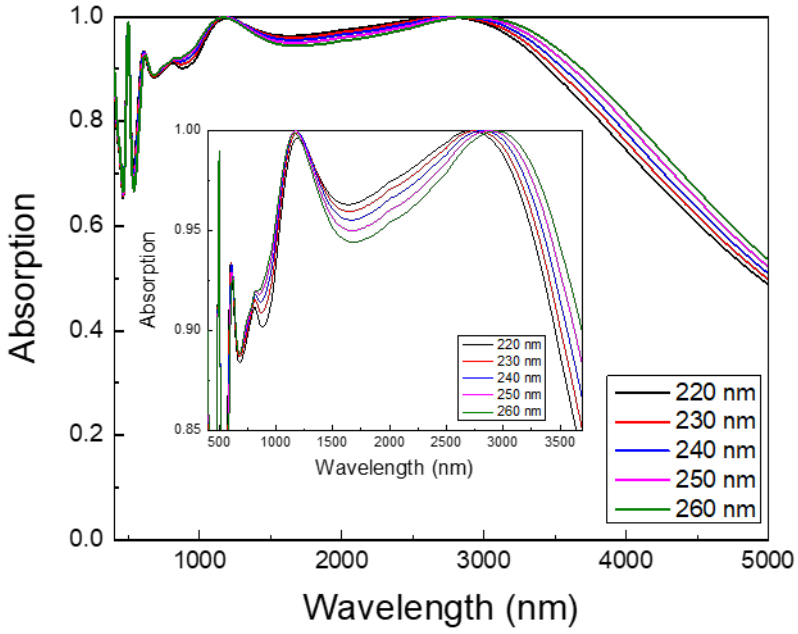

Fig. 2. Effect of side length of two-layer cube on absorption rate of designed absorber.

Fig. 2 also illustrates that the absorption peaks within the wavelength range of 2500 to 3250 nm exhibited an absorption rate exceeding 99%. These peaks were specifically identified within the following wavelength ranges: 2390 to 2980 nm, 2420 to 3020 nm, 2460 to 3100 nm, 2520 to 3170 nm, and 2600 to 3250 nm. Notably, the absorption peaks within the 2500–3200 nm range display a noticeable red shift with the shift progressing from 2650 to 2950 nm as the cube's side length increases from 220 to 260 nm. Conversely, the absorption peaks at 490, 610, 820, and 1170 nm do not exhibit red-shifted characteristics with increasing side lengths. These outcomes confirmed that the absorption peaks observed in the 2500–3200 nm range originated from the PSP resonance phenomenon, which substantiated the high absorption capabilities of the designed ultra-broadband absorber across a wide spectrum.

We analyzed the absorption spectrum of the absorber with and without the uppermost Al_2O_3 layer (t1) when subjected to normal incident light. The purpose of this simulation was to demonstrate the anti-reflection effect of the uppermost Al_2O_3 layer. The results, depicted in Fig. 3, revealed distinctive absorption peaks in the absorption spectra of the uppermost Al_2O_3 layer at 490, 610, 820, 1280, and 2880 nm. Comparing the absorber with and without the anti-reflection Al_2O_3 layer, we observed that the absorber

with the anti-reflection layer exhibited higher absorption rates in the visible region. Specifically, for the absorbers featuring anti-reflective Al_2O_3 layers, the absorptivity exceeded 90% within the wavelength range of 600 to 3650 nm. Additionally, we observed absorption peaks at 1170 and 2880 nm, where the absorptance surpassed 99%. These findings indicated that the absorber with the studied anti-reflective Al_2O_3 layer demonstrated perfect absorption characteristics at these particular wavelengths. For the absorber without the Al_2O_3 layer, the absorption rate at 2880 nm exceeded 99%, but a high absorption rate of over 90% occurred only within a narrow range. Additionally, in the wavelength range of 600 to 2300 nm, the absorption rate was significantly lower compared to the absorber with an anti-reflection layer. These findings highlighted the role of the uppermost Al_2O_3 cubic layer as an antireflection layer, which enhanced absorption across a broad wavelength range.

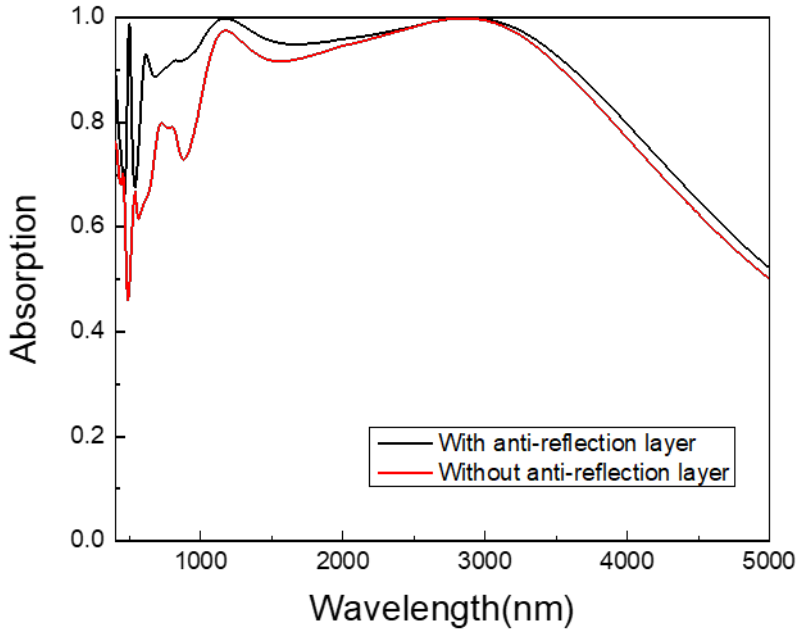

Fig. 3. Absorbers with Al_2O_3 antireflection layer (black line) and without antireflection layer (red line).

When the uppermost layer of Al_2O_3 cubes functioned as the antireflection layer, the simulation results aligned with expectations, showing that the absorber achieved higher absorption rates across the entire simulated region (400–5000 nm) compared to the absorber without the Al_2O_3 antireflection layer. The results implied that the inclusion of the Al_2O_3 antireflection layer significantly improved the performance of the absorber. By acting as an antireflection coating, the Al_2O_3 layer minimized the reflection of the incident light, allowing a larger portion of the light to be absorbed by the absorber material. This effect was particularly evident in the broader wavelength range of 600 to 2300 nm, where the absorber with the Al_2O_3 layer outperformed the absorber without it. The enhanced absorption characteristics provided by the Al_2O_3 layer were of great significance in various applications such as photovoltaic devices or optical sensors. The ability to maximize light absorption across a wide range of wavelengths contributes to improved energy conversion efficiency and sensitivity in these devices. These findings underscored the importance of antireflection layers in optimizing the performance of absorbers and highlighted the potential for further advancements in absorber design by leveraging materials such as Al_2O_3 to enhance light absorption. Future research is necessary to explore additional modifications or combinations of materials to achieve even higher absorption rates and broader spectral coverage, leading to improved efficiency and performance in various applications.

To demonstrate the superiority of the designed absorber which consisted of two layers of square cubes stacked on four layers of square continuous planar film, we conducted a comparative analysis with a six-layer planar continuous film absorber as illustrated in Fig. 4. The structures were simulated, and compared accordingly. Each layer's thickness matched that of the absorber depicted in Fig. 1. As depicted in Fig. 4, the six-layer planar continuous film absorber exhibited a sharp absorption peak in broadband. However, the absorption peaks observed at 490, 610, 820, 1170, and 2280 nm in the designed absorber's absorption spectrum were not present in the six-layer planar continuous film absorber. Furthermore, the six-layer planar continuous film absorber achieved a maximum absorption rate of 88% at 1200 nm but failed to sustain an absorption rate above 90% across the entire wavelength range. This result was attributed to the combined effect of localized surface plasmon (LSP) resonance and propagating surface plasmon (PSP) generated on the Al_2O_3-Ti film within the six-layer planar continuous film absorber.

Fig. 1 shows the formation of two Fabry-Perot (FP) resonant cavities using different layers. The first cavity consisted of a Ti square cube (t2) separated by a PNIPAAm layer and a Ti planar thin film layer (t4). The second cavity was formed by two Ti planar thin film layers (t4 and t6) separated by a SiO_2 layer. The results presented in Fig. 6 support the excitation of the LSP resonance in the Al_2O_3 (t1)-Ti (t2) cube and the LSP and FP cavity resonances in the Ti (t2)-PNIPAAm (t3)-Ti (t4)-SiO_2 (t5)-Ti (t6) layer. These findings indicated that the proposed structure simultaneously excited multiple electromagnetic resonance modes. Consequently, the absorptivity and average absorptivity of the designed absorber were superior to those of the six-layer planar continuous film absorber. This comparison provides compelling evidence for the enhanced resonant absorption in the red and near-infrared regions of the analyzed wavelengths due to the synergistic resonance effects of the LSP and FP resonators.

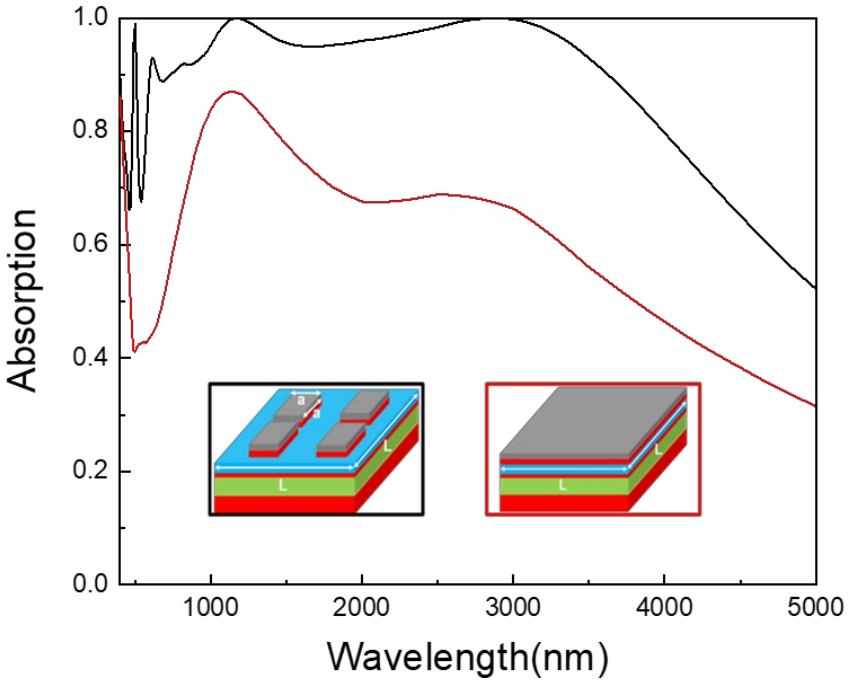

Fig. 4. Designed absorber (black line) and six-layer planar continuous film absorber (red line).

We analyzed the distribution of electric field strength (|E|) and magnetic field strength (|H|) in the *x*-*z* plane at various wavelengths. The corresponding results are presented in Figs. 5 and 6, respectively. To initiate the experimental setup, we employed vertically incident TE light as the light source to stimulate the operation of the designed absorber. The absorption spectrum depicted in Fig. 4 (middle) revealed absorption peaks at 490, 610, 820, 1170, and 2280 nm. These wavelengths coincided with the excitation wavelengths observed during the experiments. When the incident light excited positive and negative film dielectric constant materials continuously on the surface, it triggered a PSP resonance between the interfaces due to the conduction electron resonance oscillation. Fig. 5 displays the electric field intensity distribution under vertically incident TE light at different wavelengths. The intensity was coupled at the edge of the first Al_2O_3 layer, which was situated in the gap between the two layers of square cubes. It then permeated through the PNIPAAm layer into the SiO_2 layer, ultimately reaching the reflective bottom Ti layer. Thus, this absorber exhibited distinct surface plasmon resonances and a strong electric field not only on the top of the Al_2O_3-Ti cube but also simultaneously below the four continuous films.

The electric field shown in Fig. 4 is predominantly concentrated at the edges and inside of the top Al_2O_3-Ti cube. Additionally, for incident light with wavelengths of 490, 610, 820, and 1170 nm, the electric field was distributed within the PNIPAAm and SiO_2 layers. Notably, when the excitation light had a wavelength greater than 250 nm, LSP resonance occurred in both the two-layer Al_2O_3 square cube and the Ti square cube. However, the intensity of the LSP resonance depended on the incident light wavelength and the size of the nanostructure or nanoparticle material being designed. By examining the result shown in Fig. 5 which displays incident light wavelengths of 490, 610, 820, and 1170 nm, it was evident that a strong electric field emerged in the neighboring regions of the Al_2O_3 and Ti square cubes. These observations indicated that the significant absorption of incident light at 490, 610, 820, and 1170 nm was attributed to the excitation of the absorbers being studied, brought about by distinct plasmonic resonances. The initial resonance occurred between the top Al_2O_3-Ti square cube layer and the metallic Ti film, followed by the subsequent FP cavity resonance in the PNIPAAm and SiO_2 layers.

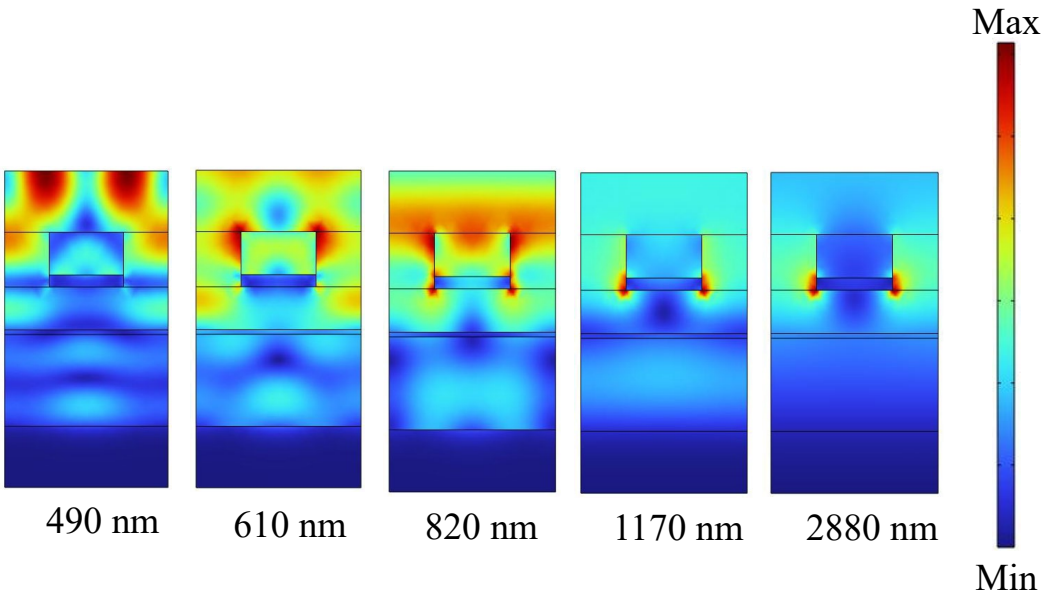

Fig. 5. Electric field intensity distribution under normal incident TE light with different excitation wavelengths.

Fig. 6 presents the magnetic field distributions at various excitation wavelengths, namely 490, 610, 820, 1170, and 2880 nm. The results demonstrated that the magnetic fields corresponding to different excitation wavelengths were present in both the Al_2O_3 and Ti square cubes, as well as in the PNIPAAm and SiO_2 dielectric layers. The configuration consisted of two FP resonant cavities formed by the t2–t4 and t4–t6 Ti metal layers, which were separated by the PNIPAAm and SiO_2 layers. When the excitation wavelengths of 490, 610, 820, and 1170 nm satisfied the FP cavity resonance condition, the incident light interacted constructively or destructively with the reflected light. Consequently, the magnetic field distribution indicated the successful excitation of the FP cavity resonance in the PNIPAAm and SiO_2 dielectric layers. Furthermore, the result in Fig. 6 also revealed that the excitation of the FP cavity resonance varied the strengths of the magnetic field distribution within the PNIPAAm and SiO_2 layers owing to the distinct excitation wavelengths employed. This observation demonstrated that the FP cavity resonance induced different intensities of the magnetic field distribution. Additionally, the excitation wavelengths of 490, 610, 780, 820, and 1170 nm also activated LSP resonances in the Al_2O_3-Ti square cubes.

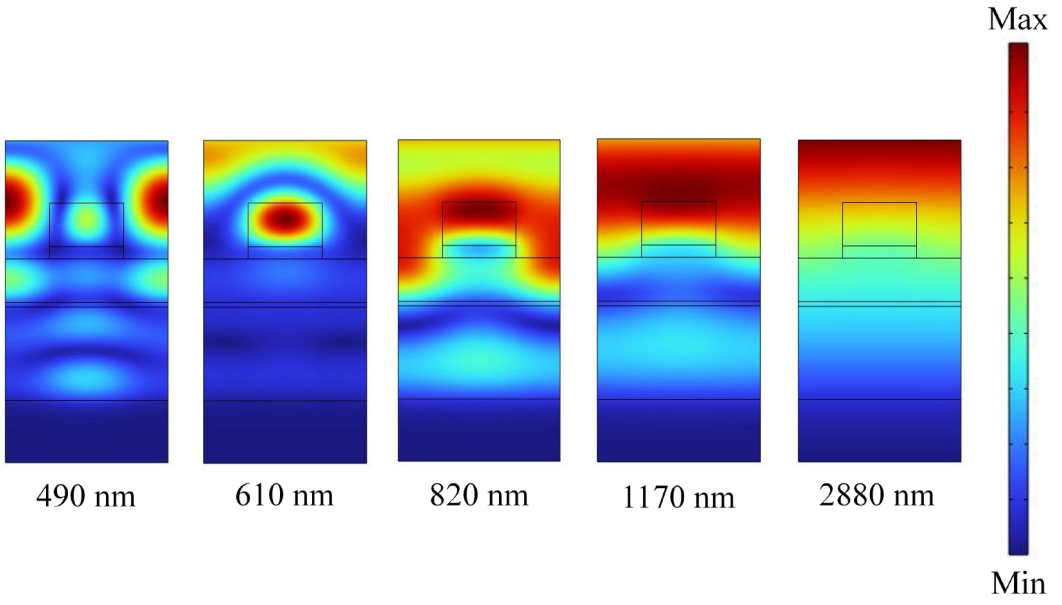

Fig. 6. Magnetic field intensity distribution under normal incident TE light with different excitation wavelengths.

The incident light underwent reflection between the metal layers t2–t4 of the PNIPAAm dielectric layer, resulting in a significant distribution of magnetic field between the metal layers t4–t6 of the SiO2 dielectric layer. This interaction between layers raised absorption peaks at approximately 610 and 820 nm owing to a combination of LSP and FP cavity resonances. When considering normal incident light with a wavelength of 2880 nm, the electric field was distributed around the double-layered square cube structure, while the magnetic field was distributed across the entire absorber area under investigation. As a result, the excellent absorption observed at wavelengths around 2880 nm can be primarily attributed to the plasmon-induced transparency (PSP) resonance occurring throughout the absorber. These findings further confirmed that the strong absorption observed across a wide range of wavelengths was a consequence of the combined effects of LSP, PSP, and FP cavity resonances.

Fig. 7 shows the changes in the absorption performance of incident light from 0 to 50° under TE polarization. In the range of 0 to 35°, the absorber demonstrated exceptional absorption capabilities, absorbing over 90% of the incident light across the spectral range of approximately 700 to 3500 nm. Moreover, when the incident light was at a larger angle of 40°, the designed absorber maintained over 90% absorption within the range of approximately 1000 to 3500 nm, exhibiting a broad bandwidth near 2500 nm. Furthermore, at a significant incident angle of 50°, the absorber exhibited over 80% absorption within the range of approximately 1200 to 3600 nm, boasting a wide bandwidth near 2400 nm. These findings demonstrated the insensitivity of the designed absorber to incident angles, thereby highlighting its robust performance across a variety of viewing angles.

Fig. 8 illustrates the impact of different polarization angles on the absorption performance of the absorber. A polarization angle of 0° corresponded to TE polarization, where the incident light's polarization direction aligned with the X direction. Similarly, a polarization angle of 90° corresponded to TM polarization with the incident light's polarization direction aligned with the *y* direction. The absorptivity distribution (Fig. 8) revealed that the absorptivity remained relatively stable as the polarization angle increases from 0 to 90°. This indicated that the absorption performance remained unaffected by changes in the polarization angle. The observed polarization independence highlighted the high absorption efficiency of the studied absorber. Consequently, this characteristic enhanced the practical value and applicability of the absorber in real-world scenarios. The polarization-independent nature of the absorber was particularly advantageous in practical applications. It ensured consistent absorption performance regardless of the incident light's polarization direction. This also broadened the range of potential applications for the studied absorber and enhances its suitability for various practical use cases.

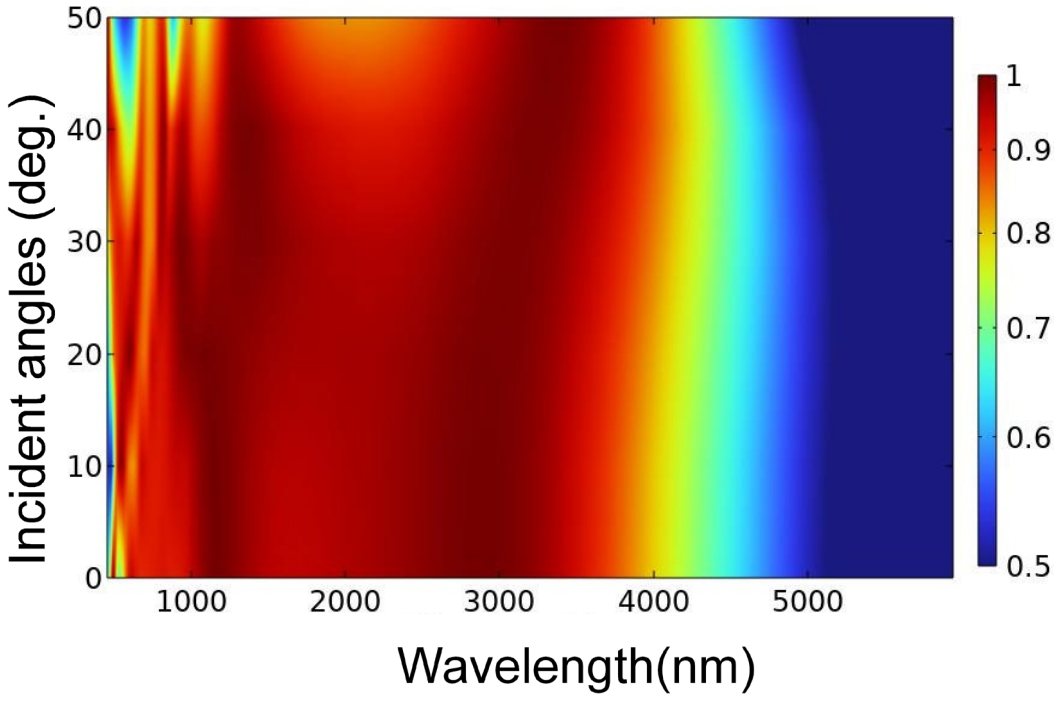

Fig. 7. Changes in absorption properties of incident light from 0 to 50° under TE polarization.

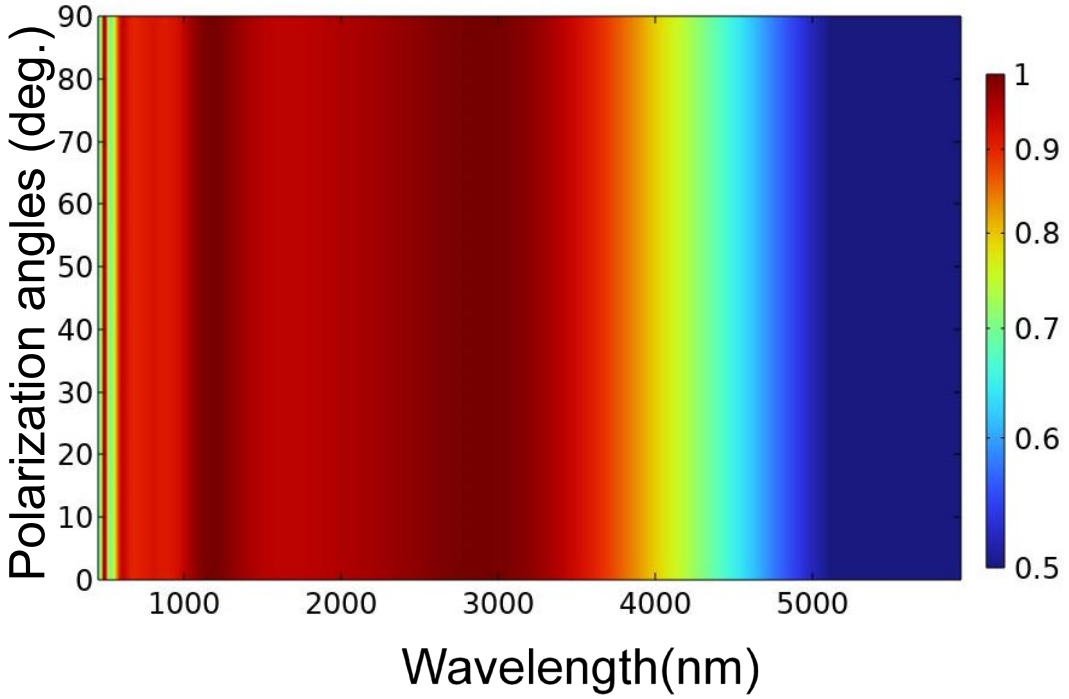

Fig. 8. Changes in absorbance at different polarization angles.

4. Conclusions

For a newly designed absorber for solar energy production, we analyzed the impact of parameters and geometries on the absorption performance of different structures using COMSOL finite element analysis software. The absorption spectrum of the absorber revealed distinct peaks at 490, 610, 820, 1170, and 2880 nm. We observed a noticeable red shift in the absorption peak within the wavelength range of 2500 to 3200 nm as the side length of the cube increased from 220 to 260 nm. This shift occurred from 2650 to 2950 nm, providing evidence that the absorption peak is a result of PSP resonance. By incorporating an anti-reflection Al_2O_3 cubic layer, as well as PSP, LSP, and FP cavity resonances in the absorber layer, the characteristics of ultra-broadband absorption and multiple absorption peaks were found, resulting in a high absorption rate. Data analysis results revealed that the designed ultra-broadband absorber achieved an absorption rate exceeding 90%. The average absorption rate within 600 to 3650 nm reached 96.3% with a maximum absorption rate of 99.9%. Furthermore, the absorber demonstrated high absorptivity for TE and TM polarized light at a 90° incident angle, maintaining an absorptivity exceeding 90% within the desired bandwidth. Overall, the designed absorber exhibited advantages of ultra-broadband absorption, a simple structure, and polarization insensitivity.

Author Contributions: Conceptualization, D. Yang and C.F. Yang; methodology, D. Yang, L.C. Tseng, W.Z. Li and C.F. Yang; software, D. Yang, L.C. Tseng, W.Z. Li and C.F. Yang; validation, D. Yang, L.C. Tseng, W.Z. Li and C.F. Yang; formal analysis, D. Yang, L.C. Tseng, W.Z. Li and C.F. Yang; data curation, D. Yang, L.C. Tseng, W.Z. Li and C.F. Yang; writing—original draft preparation, D. Yang and C.F. Yang; writing—review and editing, D. Yang and C.F. Yang; visualization, D. Yang, L.C. Tseng, W.Z. Li and C.F. Yang. All authors have read and agreed to the published version of the manuscript.

Funding: Please add: This research received no external funding.

Acknowledgments: We would like to thank Pitotech Co. LTD for their help in teaching the use of COMSOL Multiphysics® software.

Conflicts of Interest: The authors declare no conflict of interest.

References

1. Landy, N.I.; Sajuyigbe, S.; Mock, J.J.; Smith, D.R.; Padilla, W.J. Perfect metamaterial absorber. *Physical Review Letters* **2008**, *100*, 207402.
2. Liu, N.; Mesch, M.; Weiss, T.; Hentschel, M.; Giessen, H. Infrared Perfect Absorber and Its Application As Plasmonic Sensor. *Nano Letters* **2010**, *10*, 2342–2348.
3. Chen, K.; Adato, R.; Altug, H. Dual-Band Perfect Absorber for Multispectral Plasmon-Enhanced Infrared Spectroscopy. *ACS Nano* **2012**, *6*, 7998–8006.

4. Shen, X; Cui, T.J.; Zhao, J.; Ma, H.F.; Jiang, W.X.; Li, H. Polarization-independent wide-angle triple-band metamaterial absorber. *Optics Express* **2011**, *19*, 9401–9407.
5. Baqir, M.A.; Choudhury, P.K. Hyperbolic Metamaterial-Based UV Absorber. *IEEE Photonics Technology Letters* **2017**, *29*, 1548–1551.
6. Li, W.; Guler, U.; Kinsey, N.; Naik, G.V.; Boltasseva, A.; Guan, J.; Shalaev, V.M.; Kildishev, A.V. Refractory Plasmonics with Titanium Nitride: Broadband Metamaterial Absorber. *Advance Materials* **2014**, *26*, 7959–7965.
7. Park, H.; Lee, S.Y.; Kim, J.; Lee, B.; Kim, H. Near-infrared coherent perfect absorption in plasmonic metal-insulator-metal waveguide. *Optics Express* **2015**, *23*, 24464–24474.
8. Watts, C.M.; Liu, X.; Padilla, W.J. Metamaterial Electromagnetic Wave Absorbers. *Advance Materials* **2012**, *24*, OP98–OP120.
9. Liu, J.; Ma, W.Z.; Chen, W.; Yu, G.X.; Chen, Y.S.; Deng, X.C.; Yang, C.F. Numerical analysis of a novel ultra-wideband metamaterial absorber with high absorptivity from visible light to near-infrared. *Optics Express* **2020**, *28*, 23748–23760.
10. Chen, W.; Liu, J.; Ma, W.; Yu, G.X.; Chen, J.Q.; Cai, H.; Yang, C.F. Numerical Study of Multilayer Planar Film Structures for Ideal Absorption in the Entire Solar Spectrum. *Applied Sciences* **2020**, *10*, 3276.
11. Zhou, Y.; Qin, Z.; Liang, Z.; Meng, D.; Xu, H.; Smith, D.R.; Liu, Y. Ultra-broadband metamaterial absorbers from long to very long infrared regime. *Light: Science Applied* **2021**, *10*, 138.